AGU PUBLICATIONS

JGR

Journal of Geophysical Research: Space Physics

RESEARCH ARTICLE
10.1002/2015JA021359

Key Points:
- Detailed study of MGS observations of the Martian magnetotail
- We find a correlation between the IMF direction and the location of its lobes
- Results compatible with analytical model of draping from first principles

Correspondence to:
N. Romanelli,
nromanelli@iafe.uba.ar

Citation:
Romanelli, N., C. Bertucci, D. Gómez, and C. Mazelle (2015), Dependence of the location of the Martian magnetic lobes on the interplanetary magnetic field direction: Observations from Mars Global Surveyor, *J. Geophys. Res. Space Physics*, *120*, 7737–7747, doi:10.1002/2015JA021359.

Received 21 APR 2015
Accepted 28 AUG 2015
Accepted article online 3 SEP 2015
Published online 30 SEP 2015

Dependence of the location of the Martian magnetic lobes on the interplanetary magnetic field direction: Observations from Mars Global Surveyor

N. Romanelli[1], C. Bertucci[1], D. Gómez[1], and C. Mazelle[2,3]

[1]Institute for Astronomy and Space Physics, Ciudad Universitaria, Buenos Aires, Argentina, [2]CNRS, IRAP, Toulouse, France, [3]Université Paul Sabatier, IRAP, Toulouse, France

Abstract We use magnetometer data from the Mars Global Surveyor (MGS) spacecraft during portions of the premapping orbits of the mission to study the variability of the Martian-induced magnetotail as a function of the orientation of the interplanetary magnetic field (IMF). The time spent by MGS in the magnetotail lobes during periods with positive solar wind flow-aligned IMF component $B_{\parallel}^{IMF}$ suggests that their location as well as the position of the central polarity reversal layer (PRL) are displaced in the direction antiparallel to the IMF cross-flow component $B_{\perp}^{IMF}$. Analogously, in the cases where $B_{\parallel}^{IMF}$ is negative, the lobes are displaced in the direction of $B_{\perp}^{IMF}$. This behavior is compatible with a previously published analytical model of the IMF draping, where for the first time, the displacement of a complementary reversal layer (denoted as IPRL for inverse polarity reversal layer) is deduced from first principles.

1. Introduction

Among other important results, the measurements made by the magnetometer (MAG) on board the Mars Global Surveyor (MGS) spacecraft [*Acuña et al.*, 1992] showed that Mars does not have a significant intrinsic magnetic field [*Acuña et al.*, 1998]. As a consequence, there is a direct interaction between the magnetized solar wind (SW) and the atmosphere/ionosphere of the planet. As part of this interaction, the atmosphere of Mars is subject to ionizing mechanisms such as photoionization, charge exchange, and electron impact. Also, through several current systems, it generates perturbations in the streaming interplanetary magnetic field (IMF), leading to its draping around the Martian effective conducting surface. In the locations where the collisionless regime holds, the plasma that is frozen into the IMF piles up in front of the stagnation region of the flow and drapes around the body while the flow is diverted around the object. These processes establish an induced magnetic tail in the downstream sector formed by two lobes of opposite magnetic polarity and separated by a polarity reversal layer (PRL). Within our own solar system a variety of objects such as active comets, Venus, and Saturn's satellite Titan perturb the streaming magnetized plasma in a way similar to Mars, thus suggesting that common physical processes are at work. The main properties of the interaction between the SW and active comets are described in *Schmidt and Wegmann* [2013]. In particular, the structure of cometary plasma tails introduced by *Alfven* [1957] has been confirmed by the magnetic field measurements collected by various spacecraft. Observations of the International Cometary Explorer across the magnetotail of comet Giacobini-Zinnner [*Slavin et al.*, 1986] revealed a well-defined two-lobe structure with a plasma sheet with a factor of 2 difference between the magnetic field strength in the outer parts of the lobes and the central tail. In addition, these measurements also revealed a well-defined outer boundary.

An extensive review on the different regions and boundaries of the induced magnetospheres of Mars, Venus, and Titan together with a comparison between them can be found in *Bertucci et al.* [2011]. The induced magnetotail of Venus has been extensively studied by Pioneer Venus Orbiter (PVO) and Venus Express spacecrafts [*McComas et al.*, 1986; *Saunders and Russell*, 1986; *Zhang et al.*, 2010]. In particular, *McComas et al.* [1986] determined the average structure of Venus magnetotail in the range between 8 and 12 Venusian radii (R_V, with $R_V = 6052$ km) downstream from the planet from PVO magnetometer observations. The authors found that the magnetotail structure consisted of two opposite pointing magnetic lobes separated by a layer whose location was displaced in approximately 0.5 R_V in the cross-SW flow direction. They found this observation to be consistent with the IMF component parallel to the SW, for a nominal Parker spiral pattern. Additionally,

Zhang et al. [2010] reported asymmetries in the lobes with respect to the orientation of the interplanetary convective electric field.

Concerning Titan, from the very beginning Cassini magnetometer observations confirmed the presence of a bipolar-induced magnetic tail with a well-defined PRL [*Backes et al.*, 2005]. A similar configuration was found for flybys at even greater distances from the moon [*Bertucci et al.*, 2007]. More recently, *Simon et al.* [2013] published a comprehensive analysis of the draping of Saturn's magnetic field around Titan as a function of the direction of the external magnetic field. In their study of the location of the PRL, the authors used an empirical relationship for the tilt of the PRL with respect to the plane containing the center of the body that is parallel to the one generated by the upstream magnetic field and velocity [*Simon and Motschmann*, 2009]. In the case of Titan, the external flow is essentially the Kronian plasma stream, while for Mars and Venus it is simply the SW. Unique observations reveal that the external flow for Titan can also be the SW [*Bertucci et al.*, 2015].

In a similar way to Venus, the Martian-induced magnetosphere is first preceded by a bow shock (BS) owing to the supersonic nature of the SW. Downstream of this boundary is the Martian magnetosheath, a region characterized by a strong wave activity where the SW is heated and slowed down. An inner boundary—often referred to as the magnetic pileup boundary or MPB—is the outer limit of the induced magnetosphere in the dayside/upstream hemisphere. The magnetotail is contained within the magnetic tail boundary, which is connected to the MPB on the dayside. In the magnetic pileup region located right inside the MPB, both the field strength and the field line draping increase significantly [*Bertucci et al.*, 2003]. Initial observations [*Yeroshenko et al.*, 1990] by Phobos-2 magnetometer acquired during four orbits at 2.86 Martian radii (R_M, where 1 R_M = 3390 km) showed that the Martian magnetotail consists of away and toward lobes containing, respectively, draped IMF lines parallel and antiparallel to the external SW flow. However, the question of the existence of an intrinsic magnetic field was unresolved at that time. With the arrival of MGS at Mars and the confirmation of the absence of an intrinsic magnetic field, MAG measurements were used to characterize the IMF draping. In particular, *Crider et al.* [2004] provided an analysis of the geometry of the magnetic field with respect to the orientation of the IMF upstream. In order to do so, the authors applied the Rankine-Hugoniot shock jump relations to MGS observations to obtain the upstream field from MGS MAG measurements in the magnetosheath.

Although several publications address the draping of an external field around a conducting obstacle from numerical simulations [*Dursi and Pfrommer*, 2008], only a few theoretical works treat this effect in detail. In an attempt to study this process from first principles, *Romanelli et al.* [2014] analytically solved the ideal problem of a perfectly conducting magnetized plasma flow around a spherical body for an arbitrary angle between the upstream flow velocity and the magnetic field vectors. Because of the linearity of the idealized problem with respect to the magnetic field (they considered the velocity field as given), the general solution for any possible angle between both fields (boundary condition) can be derived from the linear combination between two solutions associated with the strictly parallel and the strictly perpendicular cases. The authors found that when the external magnetic field is strictly perpendicular to the direction of the flow, the induced magnetic tail formed downstream from the obstacle consists of two mirror-symmetric magnetic hemispheres separated by a flat PRL, which is normal to the $B_{\perp}^{\mathrm{IMF}}$ direction and contains the $B_{\parallel}^{\mathrm{IMF}}$ vector (see also *Dursi and Pfrommer* [2008] for this particular case). However, if the IMF component along the external flow direction $B_{\parallel}^{\mathrm{IMF}}$ is nonzero, the mirror symmetry breaks down, giving rise to an inverse polarity reversal layer (IPRL) whose location depends on the orientation of the background magnetic field. The IPRL is defined by the loci of all the points where the magnetic field component parallel to the flow changes sign in a sense opposite to that in the PRL. Furthermore, *Romanelli et al.* [2014] show that the IPRL displacement will be along the IMF cross-flow component $B_{\perp}^{\mathrm{IMF}}$ for negative $B_{\parallel}^{\mathrm{IMF}}$, whereas it will be antiparallel to $B_{\perp}^{\mathrm{IMF}}$ for positive $B_{\parallel}^{\mathrm{IMF}}$. In this regard, even though *Romanelli et al.* [2014] did not compute the shift associated with the PRL (because of the absence of resistivity), the fact that the solution for the magnetic field is the result of the solution of the purely perpendicular and the purely parallel cases shows that the sign of the latter controls the direction of the shift of the magnetic lobes. Moreover, since the inclusion of resistivity effects do not break the mirror symmetry observed under a strictly perpendicular case, the shift of the PRL for other magnetic field orientations (for a fixed velocity field) must take place in the same direction than that of the IPRL.

For the sake of clarity, let us consider an example regarding the expected magnetic field morphology within the Martian-induced magnetosphere. Based on the previous theoretical results, the induced magnetotail lobes, the PRL and the IPRL should be displaced to either side of the Mars-SW flow line, with the sense and

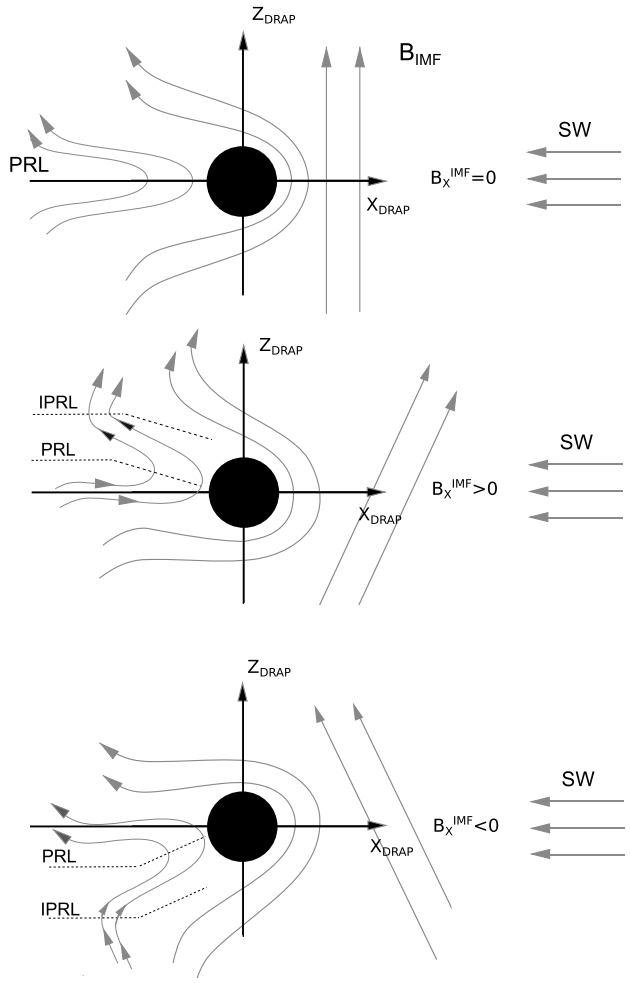

Figure 1. Scheme of an induced magnetosphere for different IMF orientations seen from the DRAP coordinate system. In all panels the solar wind flows antiparallel to the *X* axis and the *Z* component of the IMF is positive. The PRL is located between both magnetic lobes (where $B_{XDRAP} = 0$). (top) $B^{IMF}_{XDRAP} = 0$, (middle) $B^{IMF}_{XDRAP} > 0$, and (bottom) $B^{IMF}_{XDRAP} < 0$. The PRL is located at $Z = 0$, in the northern and the southern hemisphere, respectively. Figure based on *Simon et al.* [2013]. For the computation of the location of the IPRL, the reader is referred to *Romanelli et al.* [2014].

magnitude of the displacement being controlled by the orientation of the IMF. As a consequence of this, two magnetic polarities are then expected to be observed on one hemisphere of the $(\mathbf{V_{SW}} \times \mathbf{B^{IMF}}) - \mathbf{V_{SW}}$ plane, while only one polarity is expected to be present on the other side.

Figure 1 presents a scheme for an induced magnetosphere for different IMF orientations showing the three possible scenarios mentioned above (in the top, middle, and bottom, respectively) as seen in a "draping" (DRAP) coordinate system, where the *X* axis is antiparallel to the external SW flow and the *Z* axis is parallel to $B^{IMF}_{\perp}$. If we focus on the tail ($X_{DRAP} < 0$), a few conclusions can be drawn from this figure:

1. If $B^{IMF}_{XDRAP} = -B^{IMF}_{||} = 0$, negative B_{XDRAP} values are restricted to the $Z_{DRAP} > 0$ sector. Conversely, positive B_{XDRAP} values will be confined to locations where $Z_{DRAP} < 0$.
2. If $B^{IMF}_{XDRAP} = -B^{IMF}_{||} > 0$, every location with $Z_{DRAP} < 0$ will display positive B_{XDRAP}. However, regions with $Z_{DRAP} > 0$ will display both positive and negative B_{XDRAP} values.
3. If $B^{IMF}_{XDRAP} = -B^{IMF}_{||} < 0$, every location with $Z_{DRAP} > 0$ will display negative B_{XDRAP}. However, regions with $Z_{DRAP} < 0$ will display both positive and negative B_{XDRAP} values.

In order to investigate whether the above correlation between the spatial distribution of the Martian magnetic lobes and the IMF orientation is observed in the induced magnetosphere of Mars, we analyze MGS MAG data obtained during the mission's premapping orbits (first aerobraking phase or AB1 and science phasing orbits

or SPO). In these periods, the spacecraft completed 570 elliptical orbits during which it sampled both the upstream and the magnetotail regions.

This study is structured as follows: a brief description of the capabilities of the magnetometer on board MGS and the reliability of the magnetic field measurements are presented in section 2. The selection criteria applied to MAG data to analyze the relationship between the interplanetary magnetic field direction and the spatial location of the Martian magnetic lobes are introduced in section 3. In section 4 we derive the properties of the IMF for the previously selected orbits. Additionally, we perform a statistical study of the position of the magnetic lobes with respect to a coordinate system that takes into account the IMF orientation. In section 5 we summarize our conclusions.

2. Instrument Description

Mars Global Surveyor arrived at Mars on 11 September 1997. Next, MGS was placed in highly elliptical orbits providing measurements of the Martian environment from the unperturbed solar wind down to the planet's neutral atmosphere. The evolution of MGS orbital period through the premapping aerobraking and SPO phases is presented in detail in *Albee et al.* [2001]. During AB1, which took place between Mars orbit insertion and April 1998, MGS's orbital period was reduced from 48 to 12 h. SPO came in after AB1 and ended in November 1998, when a second aerobraking phase began. SPO orbits had a constant period of approximately 12 h, apoapses above the south pole at distances of roughly 6 R_M, and local times that varied monotonically between noon and 4 A.M. After these orbital phases, MGS reached a final circular mapping orbit at 400 km altitude.

MGS carried a twin, triaxial fluxgate magnetometer system [*Acuña et al.*, 1992] which provided fast measurements (32 vectors/s) over a wide dynamic range (from ±4 nT to ±65,536 nT). Magnetic field measurements have an uncertainty of ±1 nT due to spacecraft fields [*Acuña et al.*, 2001]. The spacecraft did not carry any instruments dedicated to measure ion properties.

In this work we analyze MAG measurements projected in the aberrated Mars Solar Orbital (MSO) coordinate system with a sampling frequency of 0.33 Hz and 1.33 Hz. The coordinate system is centered on Mars with the X_{MSO} axis pointing opposite to the mean solar wind flow direction in the planet frame of reference and assuming an aberration of 4°, the Z_{MSO} axis being perpendicular to Mars's orbital plane and positive to the ecliptic north, and the Y_{MSO} axis completing the right-hand system.

3. MAG Data Analysis: Selection Criteria

3.1. Data Selection, Upstream IMF Determination

For every orbit in this study, we extracted those MAG data obtained both inside the MPB and upstream from the Martian bow shock. To that purpose, we used the MPB and BS fits by *Vignes et al.* [2000]. In addition, and to filter out the potential effects of crustal magnetic fields, we discarded all MAG measurements occurring inside the MPB for which the X_{MSO} coordinate is higher than −1.5 R_M. The justification for this criterion is based on the work by *Brain et al.* [2003]. In particular, Figure 10 of that study shows the altitude profile of the magnetic field intensity above a region containing the strongest southern crustal sources. The authors found that the magnetic field falls off fast up to a transition altitude, above which it decreases less steeply. According to that study, above this transition altitude MGS MAG measures magnetic fields convected by the magnetized SW, while signatures of crustal magnetic sources are clear below it. Finally, the authors have shown that, even though crustal sources influence the magnetic fields to different altitudes above different regions, the influence of the strongest crustal magnetic field source can extend up to 1400 km (i.e., ∼ 0.41 R_M).

To determine the upstream IMF, we compute the average from the first 1000 magnetic field measurements outside the BS fit [*Vignes et al.*, 2000]. Depending on the data gaps, there are orbits with inbound and outbound IMF estimates and orbits with only one IMF estimate (obtained in only one of the two legs). This procedure ensures that the IMF is determined from an average over planetary length scales (MGS typically travels a distance of the order of ∼1 R_M perpendicular to the X_{MSO} axis during the averaging period) and allows us to derive the mean magnetic field in approximately the same spatial regions for all orbits. It also provides an acceptable determination of the IMF since it reduces the time interval between the MAG observations obtained upstream from the Martian bow shock and the ones observed in the Martian magnetotail. Furthermore, in all the following analysis it is essential to ensure that the IMF does not vary significantly while MGS

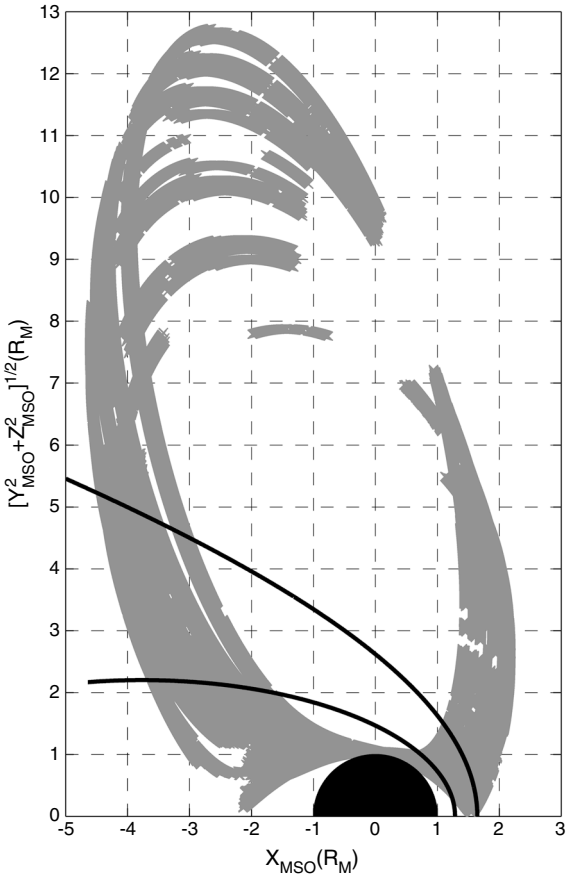

Figure 2. MGS trajectory during the selected orbits shown in the aberrated MSO cylindrical coordinate system. This coordinate system, centered at Mars, has its X_{MSO} axis pointing opposite to the mean solar wind flow direction in the planet frame of reference assuming a 4° aberration. Z_{MSO} is perpendicular to Mars's orbital plane and positive to the ecliptic north and Y_{MSO} completes the right-hand system.

crosses the magnetic tail structure. In this regard, all orbits that have two IMF estimates are better suited to test the stationarity of the IMF than those with only one estimate. Based on this point, all orbits with two clearly different IMF estimates or with one poor IMF estimate are discarded from our analysis (we get back to this point at the end of this section). As a result, we find that 71 orbits satisfy all these criteria, from which 21 have two IMF estimates. A visual inspection of the data confirms that the selection criteria are effective. Our main hypothesis is that the IMF derived for each of these orbits does not change significantly between the times where MGS is about to cross the BS and the ones where it is inside the MPB.

Figure 2 shows the trajectory of the selected orbits in the aberrated MSO cylindrical coordinate system. In all of them, MGS starts in the downstream region at very high altitudes. Then the spacecraft encounters the Martian BS (outer black line, fit from *Vignes et al.* [2000]) at locations with X_{MSO} coordinates ranging between $\sim -4.5\ R_M$ and $\sim -3.7\ R_M$. After the shock has been crossed, MGS enters the magnetosheath and reaches the MPB (inner black line, fit from *Vignes et al.* [2000]). Inside this boundary, MGS provides magnetometer measurements of the Martian magnetic lobes while approaching the planet. After closest approach has been reached, MGS crosses both boundaries again and returns to the upstream region.

3.2. Different States of the Magnetized SW: The DRAP Coordinate System

To analyze MAG observations in the magnetotail region while considering different states of the solar wind, we have performed a rotation of the coordinate system. This coordinate system, already referred to as the draping (DRAP) coordinate system [*Neubauer et al.*, 2006; *Bertucci et al.*, 2007], is defined taking into account the IMF direction as well as the SW velocity. Since MGS lacks measurements of ion properties, we assume that the solar wind flows in the aberrated Sun-Mars direction. The DRAP coordinate system is therefore defined as follows:

$$\mathbf{X_{DRAP}} = \mathbf{X_{MSO}} \tag{1}$$

$$\mathbf{Z_{DRAP}} = \frac{[\mathbf{0}, \mathbf{B_{YMSO}}, \mathbf{B_{ZMSO}}]}{\sqrt{\mathbf{B^2_{YMSO}} + \mathbf{B^2_{ZMSO}}}} \quad (2)$$

$$\mathbf{Y_{DRAP}} = \mathbf{Z_{DRAP}} \times \mathbf{X_{DRAP}} \quad (3)$$

where B_{YMSO}, B_{ZMSO} are the $Y-$ and $Z-$ MSO components of the background magnetic field calculated in the upstream region of Mars. In the case of orbits with two IMF estimates we have taken the average between both vectors. By changing from the MSO to the DRAP coordinate system, we ensure that the background magnetic field is in the $(X-Z)_{DRAP}$ plane: in the DRAP coordinate system B^{IMF}_{ZDRAP} is always positive, B^{IMF}_{XDRAP} is equal to the value of the $X-$ MSO component of the IMF, and B^{IMF}_{YDRAP} is zero. For example, according to Parker's spiral angle at Mars (55°), the IMF measured at Mars projected in MSO coordinates would be $\mathbf{B^{IMF}} = |\mathbf{B^{IMF}}|\,[0.57, 0.82, 0]$. Therefore, following the transformation described above, the latter IMF value in the DRAP coordinate reference frame is $\mathbf{B^{IMF}} = |\mathbf{B^{IMF}}|\,[0.57, 0, 0.82]$. This particular IMF then corresponds to one of the cases illustrated in Figure 1 (top). Note that changing from the MSO to the DRAP coordinate reference frame requires knowing the IMF direction, but it does not depend on the magnetic field intensity. We then characterize the Martian magnetotail structure using measurements obtained for different orbits in terms of the IMF orientation, i.e, in terms of the angle between it and the $\mathbf{X_{DRAP}}$ direction. Hereafter, we denote the angle between any magnetic field measurement and the $\mathbf{X_{DRAP}}$ axis as θ. Since the spacecraft magnetic field intensity has an upper limit of 1 nT at the location of the MAG sensors [*Acuña et al.*, 2001], the maximum deviation of θ due to this artifact is $\Delta\theta = \pm \arccos[\frac{B}{\sqrt{1+B^2}}]$. In this expression and the following all magnetic field measurements are normalized to 1 nT. This leads to an uncertainty in the cone angle of the interplanetary magnetic field $\theta_{IMF} \pm \Delta\theta_{IMF}$. Additionally, the maximum deviation of the direction of the IMF component perpendicular to the $\mathbf{X_{DRAP}}$ axis ($B^{IMF}_{\perp} = B^{IMF}_{ZDRAP}$) is $\Delta\alpha = \mathrm{atan}(B^{IMF}_{\perp})^{-1}$ (with $B^{IMF}_{\perp}$ expressed in nanotesla).

Figure 3 displays the decomposition of the averaged IMF according to the DRAP coordinate system. In particular, Figure 3 (top) presents the projection of the IMF onto the $(X-Z)_{DRAP}$ plane while the lower one shows the projection onto the $(Y-Z)_{DRAP}$ plane. Since by definition, $B^{IMF}_{\perp}$ is always parallel to the $+Z_{DRAP}$ direction, the angular uncertainty in the determination of this direction, $\Delta\alpha$, generated by the spacecraft fields defines a region where the sign of the Z_{DRAP} component (of a vector position) is undefined. This region is shown in Figure 3 in grey and is bound by the straight lines $Z_{DRAP} = Y_{DRAP}/B^{IMF}_{\perp}$ and $Z_{DRAP} = -Y_{DRAP}/B^{IMF}_{\perp}$. This issue is taken into account in the analysis regarding the location of the magnetic lobes presented in the next section.

Finally, it is important to point out that all selected orbits have a well-defined IMF direction in the following sense: all orbits with an IMF estimate such that $\theta_{IMF} \pm \Delta\theta_{IMF}$ was not able to define the sign of the B^{IMF}_{XDRAP} component were discarded. In addition, we also discarded orbits with different inbound and outbound B^{IMF}_{XDRAP} signs.

Also, with regard to our criteria, we note that some poor IMF estimates, leading to exclude orbits from the analysis, might be the sole result of taking a MAG data average over magnetosheath fields. Indeed, the Martian bow shock location is highly variable. In spite of this fact, we decided to stick to this procedure to make sure that the selected orbits are a reliable and statistically significant set of data to study the dependence of the location of the Martian magnetic lobes on the IMF orientation.

Additionally, to evaluate the impact of potential IMF variabilities on shorter time scales, we determine MAG averages over data windows with 300 and 500 data points outside of the BS fit. We do not find any significant difference with the statistical results presented in the next section.

4. Results: Magnetotail Structure and Dependence on B^{IMF}_{XDRAP}

4.1. IMF Configuration

The criteria presented in the previous section allow the characterization of each of the 71 selected orbits according to the IMF cone angle θ_{IMF}, and the orientation of the DRAP coordinate system in terms of the aberrated MSO one. Due to the experimental uncertainty $\Delta\theta_{IMF}$, we first classify these orbits into two groups depending on the value of $\theta_{IMF} \pm \Delta\theta_{IMF}$. One group contains the cases with $0° < \theta_{IMF} \pm \Delta\theta_{IMF} < 90°$ and the other one contains the cases with $90° < \theta_{IMF} \pm \Delta\theta_{IMF} < 180°$. The first group is composed of 32 orbits (with $B^{IMF}_{XDRAP} > 0$), 12 of which have IMF averages from inbound and outbound measurements. The second group contains 39 orbits (with $B^{IMF}_{XDRAP} < 0$), with 9 of them having IMF averages obtained from inbound and outbound measurements.

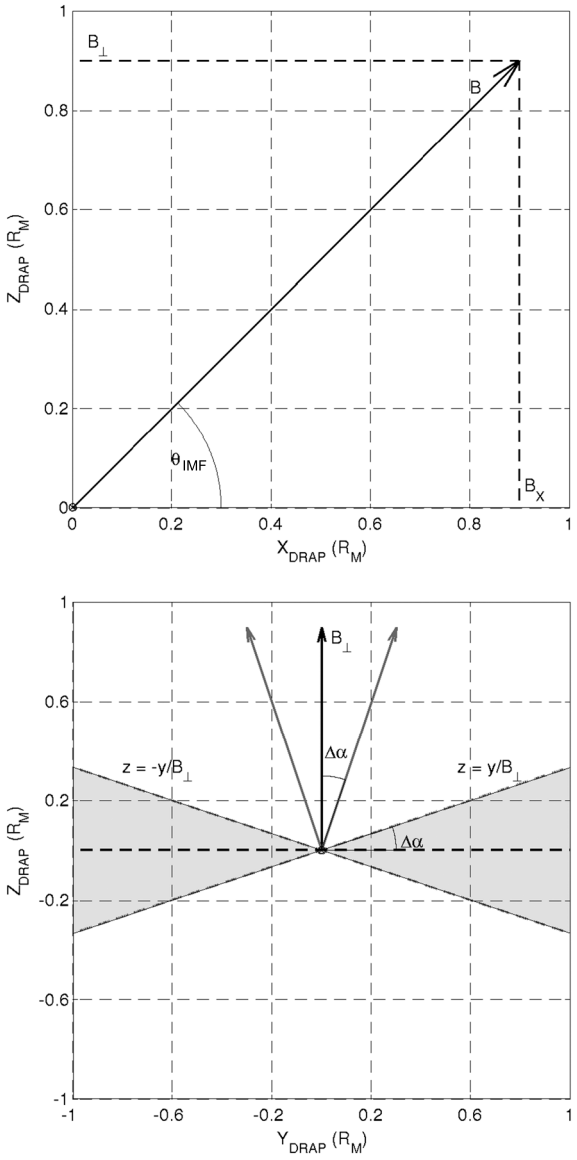

Figure 3. IMF decomposition in the DRAP system. (top) Projection onto the $(X-Z)_{DRAP}$ plane. The angle between the IMF and the X_{DRAP} axis is denoted by θ_{IMF}. (bottom) Projection onto the $(Y-Z)_{DRAP}$ plane. By definition, in the DRAP coordinate system $B_{\perp}^{IMF}$ is pointing in the $+Z_{DRAP}$ direction. $\Delta\alpha = \text{atan}\,(B_{\perp}^{IMF})^{-1}$ (with $B_{\perp}^{IMF}$ in nanotesla) is the uncertainty in the determination of this direction.

Additionally, as we have already stated in the previous section, the angular uncertainty $\Delta\alpha$ might affect the predicted location of the Martian magnetic lobes. Thus, when analyzing MAG data obtained inside the MPB, we do not consider data located inside the region limited by the straight lines $Z_{DRAP} = Y_{DRAP}/B_{\perp}^{IMF}$ and $Z_{DRAP} = -Y_{DRAP}/B_{\perp}^{IMF}$ (i.e., the grey area shown in Figure 3 (bottom)).

4.2. Magnetic Field Morphology Inside the Magnetic Pileup Boundary

In what follows we describe the observed magnetic field morphology inside the Martian magnetotail, as derived from MGS observations. Figure 4 displays the trajectory of MGS inside the MPB projected onto the $(Y-Z)_{DRAP}$ (left column) and $(X-Z)_{DRAP}$ (right column). Figure 4 (top and bottom rows) describe the location of MAG measurements under positive and negative B_{XDRAP}^{IMF} conditions, respectively. Each point represents a single MAG measurement and is color coded according to the local values of θ (0° = black, 180° = copper). These points have an associated angular uncertainty of $\Delta\theta < 20°$, ensuring that their color will not change significantly because of experimental errors.

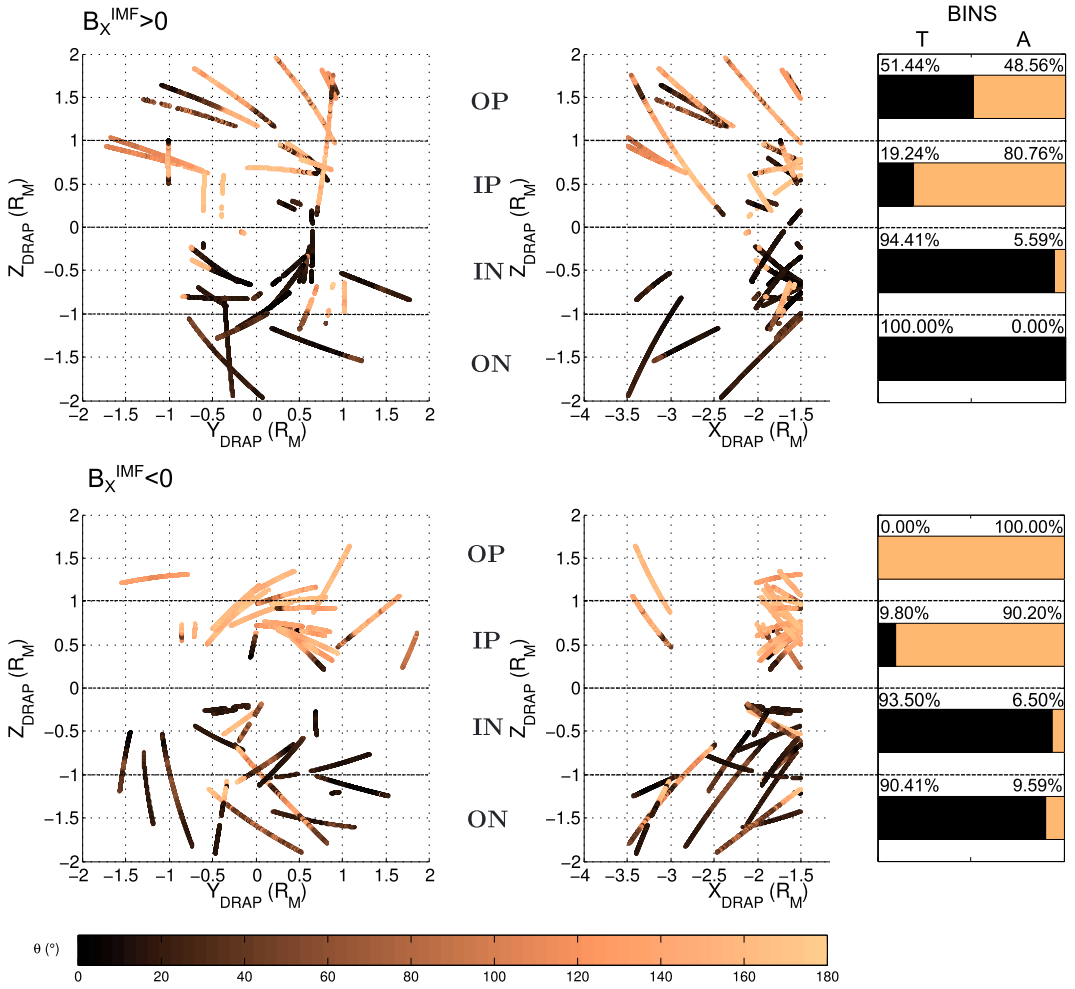

Figure 4. MGS trajectory inside the MPB projected onto the DRAP coordinate system. (top and bottom rows) Orbits with $B_{X\mathrm{DRAP}}^{\mathrm{IMF}} > 0$ ($B_{X\mathrm{DRAP}}^{\mathrm{IMF}} < 0$). (left and right columns) Projection of the trajectory of MGS in the $(Y - Z)_{\mathrm{DRAP}}$ plane ($(X - Z)_{\mathrm{DRAP}}$). The dashed lines mark the limits between the different regions inside the MPB. From the upper to the lower one, they are the outer-positive (OP), inner-positive (IP), inner-negative (IN), and outer-negative (ON) regions. The percentage bars shown at the right correspond to bins where the local magnetic field is almost antiparallel or parallel to the nominal SW flow. The T lobe and A lobe bins correspond to MAG measurements where $0° < \theta \pm \Delta\theta < 25°$ and $155° < \theta \pm \Delta\theta < 180°$, respectively.

To investigate whether there is a relationship between the spatial distribution of the Martian magnetic lobes and the IMF orientation, MGS trajectory information is additionally divided in four regions according to Z_{DRAP}. The first two regions are located inside the nominal wake. These are the inner-positive (IP) and inner-negative (IN) regions, with $0 < Z_{\mathrm{DRAP}} < 1$ and $-1 < Z_{\mathrm{DRAP}} < 0$, respectively. The remaining two regions are located outside the wake, but still within the MPB. These are the outer-positive (OP) and outer-negative (ON) regions, with $Z_{\mathrm{DRAP}} > 1$ and $Z_{\mathrm{DRAP}} < -1$, respectively.

A few features are clearly noticeable from these plots. First of all, we find that most magnetic field measurements in the lower hemisphere ($Z_{\mathrm{DRAP}} < 0$) are oriented toward the planet. Analogously, MAG measurements oriented away from Mars dominate in the upper hemisphere ($Z_{\mathrm{DRAP}} > 0$). This shows that MAG measurements are in qualitative agreement with all the schemes presented in Figure 1.

Beyond this zero-order behavior, a careful consideration of the orientation of the magnetic field in the IP, IN, OP, and ON regions under $B_x^{\mathrm{IMF}} > 0$ and $B_x^{\mathrm{IMF}} < 0$ reveals interesting features. In particular, if we consider the occurrence of fields both nearly parallel (the away lobe bin or A lobe bin) $\theta \pm \Delta\theta = [155°–180°]$ and antiparallel (the toward lobe bin or T lobe bin) $\theta \pm \Delta\theta = [0° - 25°]$ to the SW direction, we find that

1. In the ON region 100% of the magnetic field measurements belong to the toward bin (T bin) for positive B^{IMF}_{XDRAP} conditions.
2. In the ON region, ~10% of the measurements belong to the away bin (A bin) for negative B^{IMF}_{XDRAP} conditions.
3. In the OP region 100% of the MAG measurements belong to the A bin for negative B^{IMF}_{XDRAP} conditions.
4. In the OP region, ~50% of the magnetic field measurements belong to the toward bin (T bin) for positive B^{IMF}_{XDRAP} conditions.

These statistical results are displayed through the percentage bars located at the right of Figure 4. Interestingly, all these results consistently show the existence of a shift of the Martian magnetic lobes toward higher and lower values of Z_{DRAP} (with respect to the canonical position shown in Figure 1 (top)) when the B^{IMF}_{XDRAP} component is, respectively, positive or negative.

The analysis of MAG data occurring within the IP and IN regions confirms the same behavior as above, even though the trends are not as sharp as those observed in the outer regions. In the IP region both toward and away bin measurements are observed under positive B^{IMF}_{XDRAP} conditions (T bin: ~19%, A bin: ~81%). In this case, the mix is less evident than in the OP region, but still clearly showing a significant fraction of MAG measurements belonging to the T bin in the northern hemisphere. There is also a mix of T bin and A bin measurements in the IN region when $B^{IMF}_x < 0$ (T bin: 93.5%, A bin: 6.5%) and, once again, the IN region shows a lower degree of mixing when compared to the ON region. However, the observed increment in the percentage associated with the A bin going from the IN to the ON region (with $B^{IMF}_x < 0$) supports all previous results. Similarly, we do not observe 100% of the points belonging to the A bin and the T bin in the IP region (case $B^{IMF}_x < 0$) and in the IN region (case $B^{IMF}_x > 0$), respectively. However, we do observe high percentages for both cases (90.2% for the first case and 94.41% for the latter one) and we also observe 100% of the cases in the expected bins when MGS is further away from the $Z_{DRAP} = 0$ plane ($Z_{DRAP} > 1$ in the case of $B^{IMF}_x < 0$ and $Z_{DRAP} < -1$ in the case of $B^{IMF}_x > 0$).

In conclusion, there is a remarkable agreement between all the results obtained for the outer regions and the proposed theoretical explanation. Even though the expected tendencies in the inner regions are also clearly observable, we suggest that the slight deviations might be the result of the blurring produced by some of the causes discussed next. The first cause concerns the properties of the incoming solar wind. Because MGS lacks an instrument capable of measuring the SW direction, we considered that the SW flows along the Sun-Mars line, taking also into account the motion of Mars around the Sun. However, since the DRAP coordinate system orientation with respect to the aberrated MSO coordinate system depends on the direction of this flow, some of the cases that deviate from the expected trend might be (at least partially) the result of the SW not being totally aligned with the nominal Mars-Sun line. A second possible cause is related to temporal variations of the IMF. Since we analyze data provided only by one spacecraft, it is not possible to measure the IMF while MGS is inside the MPB. In this regard, even though we have performed a careful study of the MGS MAG data, analyzing orbits with two IMF derivations that do not show differences in the sign of the B^{IMF}_x component and orbits with a well-defined IMF value (inbound or outbound leg), temporal variations cannot be completely ruled out. As a result, a possible cause for the observed blurring is the flapping of the PRL (and therefore, the motion of the magnetotail lobes) in response to these temporal variations. In this regard, numerical simulations shown in *Modolo et al.* [2012] suggest that the magnetic lobes adopt a new quasi-equilibrium configuration associated with a new IMF orientation in approximately 2 min. Interestingly, the blurring is only present in two of the inner bins, but not in the outer ones. Finally, when deriving the IMF from the average of MAG MGS data during a particular data window, we are implicitly assuming that this field is uniform. Departures from this hypothesis are also able to generate deviations from the expected trend. Taking into account these factors, and the result that only 5.59% of the points in the IN bin ($B^{IMF}_x > 0$) and 9.80% in the IP bin ($B^{IMF}_x < 0$) present deviations, we conclude that there is an appreciable agreement between our results and the proposed theoretical scenario. To support the causality of the IMF orientation on the spatial location of the Martian magnetic lobes, we also find a higher percentage of T lobe cases in the IP region if $B^{IMF}_x > 0$ than in the $B^{IMF}_x < 0$ case. In the same direction but less pronounced, there is slightly higher percentage of A lobe cases belonging to the IN region if $B^{IMF}_x < 0$ than in the $B^{IMF}_x > 0$ case.

Finally, to see whether this tendency is observed even for larger bins, we perform an analogous statistical study for the angular ranges $\theta \pm \Delta\theta = [0° - 45°]$ and $\theta \pm \Delta\theta = [135° - 180°]$. Interestingly, we do not find any significant difference in the derived conclusions when using these broader bins.

5. Conclusions

In summary, in this work we find an appreciable dependence between the frequency at which the Martian magnetic lobes are observed in different spatial regions and the IMF direction. Indeed, analyses of MGS MAG data in the toward and away lobes of the Martian-induced magnetotail during periods where the SW flow-aligned IMF component is nonzero suggest that this result can be understood in terms of a displacement of the magnetic lobes that depends on the relative orientation between the IMF and the SW flow. This interpretation is in agreement with previously published studies reporting the influence of the orientation of the IMF on the location of the PRL and the IPRL [*Simon et al.*, 2013; *Romanelli et al.*, 2014] and the magnetotail lobes [*McComas et al.*, 1986].

The displacement of the magnetic lobes following the orientation of the IMF has also consequences on the location of the region where planetary particle acceleration is expected. Because of this, this effect should be taken into account when it comes to derive estimates for the planetary plasma escape rate, at least inside the magnetic pileup boundary. In this regard, simultaneous measurements in the SW region and the Martian environment or a SW monitor at the Martian orbit would be helpful to extend the analysis performed in this study and to investigate the dynamics of the induced magnetotail lobes, and their response to different configurations in the external drivers (e.g., SW speed, density, pressure, and IMF) that also vary with time.

Acknowledgments

N.R. is supported by a PhD fellowship from CONICET. The data for this study are available from the Planetary Data System (http://pds.jpl.nasa.gov). The authors acknowledge financial support from grant PICT020121763 from the Agencia Nacional de Promoción de Ciencia y Tecnología, Argentina.

Michael Liemohn thanks two anonymous reviewers for their assistance in evaluating this paper.

References

Acuña, M. H., et al. (1992), Mars observer magnetic fields investigation, *J. Geophys. Res.*, *97*(E5), 7799–7814, doi:10.1029/92JE00344.

Acuña, M. H., et al. (1998), Magnetic field and plasma observations at Mars: Initial results of the Mars Global Surveyor Mission, *Science*, *279*(5357), 1676–1680, doi:10.1126/science.279.5357.1676.

Acuña, M. H., et al. (2001), Magnetic field of Mars: Summary of results from the aerobraking and mapping orbits, *J. Geophys. Res.*, *106*(E10), 23,403–23,417, doi:10.1029/2000JE001404.

Albee, A. L., R. E. Arvidson, F. Palluconi, and T. Thorpe (2001), Overview of the Mars Global Surveyor mission, *J. Geophys. Res.*, *106*(E10), 23,291–23,316, doi:10.1029/2000JE001306.

Alfven, H. (1957), On the theory of comet tails, *Tellus*, *9*, 92–96.

Backes, H., et al. (2005), Titan's magnetic field signature during the first Cassini encounter, *Science*, *308*(5724), 992–995, doi:10.1126/science.1109763.

Bertucci, C., et al. (2003), Magnetic field draping enhancement at the Martian magnetic pileup boundary from Mars Global Surveyor observations, *Geophys. Res. Lett.*, *30*(2), 1099, doi:10.1029/2002GL015713.

Bertucci, C., F. M. Neubauer, K. Szego, J.-E. Wahlund, A. J. Coates, M. K. Dougherty, D. T. Young, and W. S. Kurth (2007), Structure of titan's mid-range magnetic tail: Cassini magnetometer observations during the T9 flyby, *Geophys. Res. Lett.*, *34*, L24S02, doi:10.1029/2007GL030865.

Bertucci, C., F. Duru, N. Edberg, M. Fraenz, C. Martinecz, K. Szego, and O. Vaisberg (2011), The induced magnetospheres of Mars, Venus, and Titan, *Space Sci. Rev.*, *162*(1–4), 113–171, doi:10.1007/s11214-011-9845-1.

Bertucci, C., D. C. Hamilton, W. S. Kurth, G. Hospodarsky, D. Mitchell, N. Sergis, N. J. T. Edberg, and M. K. Dougherty (2015), Titan's interaction with the supersonic solar wind, *Geophys. Res. Lett.*, *42*, 193–200, doi:10.1002/2014GL062106.

Brain, D. A., F. Bagenal, M. H. Acuña, and J. E. P. Connerney (2003), Martian magnetic morphology: Contributions from the solar wind and crust, *J. Geophys. Res.*, *108*(A12), 1424, doi:10.1029/2002JA009482.

Crider, D., D. Brain, M. Acuña, D. Vignes, C. Mazelle, and C. Bertucci (2004), Mars Global Surveyor observations of solar wind magnetic field draping around Mars, *Space Sci. Rev.*, *111*(1–2), 203–221, doi:10.1023/B:SPAC.0000032714.66124.4e.

Dursi, L. J., and C. Pfrommer (2008), Draping of cluster magnetic fields over bullets and bubbles-morphology and dynamic effects, *Astrophys. J.*, *677*(2), 993.

McComas, D. J., H. E. Spence, C. Russell, and M. Saunders (1986), The average magnetic field draping and consistent plasma properties of the Venus magnetotail, *J. Geophys. Res.*, *91*(A7), 7939–7953.

Modolo, R., G. M. Chanteur, and E. Dubinin (2012), Dynamic Martian magnetosphere: Transient twist induced by a rotation of the IMF, *Geophys. Res. Lett.*, *39*, L01106, doi:10.1029/2011GL049895.

Neubauer, F. M., et al. (2006), Titan's near magnetotail from magnetic field and electron plasma observations and modeling: Cassini flybys TA, TB, and T3, *J. Geophys. Res.*, *111*, A10220, doi:10.1029/2006JA011676.

Romanelli, N., D. Gómez, C. Bertucci, and M. Delva (2014), Steady-state magnetohydrodynamic flow around an unmagnetized conducting sphere, *Astrophys. J.*, *789*(1), 43.

Saunders, M. A., and C. T. Russell (1986), Average dimension and magnetic structure of the distant Venus magnetotail, *J. Geophys. Res.*, *91*(A5), 5589–5604, doi:10.1029/JA091iA05p05589.

Schmidt, H., and R. Wegmann (2013), An MHD model of cometary plasma and comparison with observations, in *Cometary Plasma Processes*, edited by A. Johnstone, pp. 49–63, AGU, Washington, D. C., doi:10.1029/GM061p0049.

Simon, S., and U. Motschmann (2009), Titan's induced magnetosphere under non-ideal upstream conditions: 3D multi-species hybrid simulations, *Planet. Space Sci.*, *57*, 2001–2015, doi:10.1016/j.pss.2009.08.010.

Simon, S., S. C. van Treeck, A. Wennmacher, J. Saur, F. M. Neubauer, C. L. Bertucci, and M. K. Dougherty (2013), Structure of titan's induced magnetosphere under varying background magnetic field conditions: Survey of cassini magnetometer data from flybys TA-T85, *J. Geophys. Res. Space Physics*, *118*, 1679–1699, doi:10.1002/jgra.50096.

Slavin, J. A., E. J. Smith, B. T. Tsurutani, G. L. Siscoe, and D. E. Jones (1986), Giacobini Zinner magnetotail: ICE magnetic field observations, *Geophys. Res. Lett.*, *13*(3), 283–286, doi:10.1029/GL013i003p00283.

Vignes, D., C. Mazelle, H. Rème, M. H. Acuña, J. E. P. Connerney, R. P. Lin, D. L. Mitchell, P. Cloutier, D. H. Crider, and N. F. Ness (2000), The solar wind interaction with Mars: Locations and shapes of the bow shock and the magnetic pile-up boundary from the observations of the mag/er experiment onboard Mars Global Surveyor, *Geophys. Res. Lett.*, *27*(1), 49–52, doi:10.1029/1999GL010703.

Yeroshenko, Y., W. Riedler, K. Schwingenschuh, J. G. Luhmann, M. Ong, and C. T. Russell (1990), The magnetotail of Mars: Phobos observations, *Geophys. Res. Lett.*, *17*(6), 885–888, doi:10.1029/GL017i006p00885.

Zhang, T. L., W. Baumjohann, J. Du, R. Nakamura, R. Jarvinen, E. Kallio, A. M. Du, M. Balikhin, J. G. Luhmann, and C. T. Russell (2010), Hemispheric asymmetry of the magnetic field wrapping pattern in the Venusian magnetotail, *Geophys. Res. Lett.*, *37*, L14202, doi:10.1029/2010GL044020.